Research Article

A 1D Model of the Arterial Circulation in Mice

Lydia Aslanidou[1], Bram Trachet[1,2], Philippe Reymond[1], Rodrigo A. Fraga-Silva[1], Patrick Segers[2] and Nikolaos Stergiopulos[1]

[1]Institute of Bioengineering, Ecole Polytechnique Fédérale de Lausanne, Lausanne, Switzerland; [2]IBiTech-bioMMeda, Ghent University-IMinds Medical IT, Ghent, Belgium

Summary

At a time of growing concern over the ethics of animal experimentation, mouse models are still an indispensable source of insight into the cardiovascular system and its most frequent pathologies. Nevertheless, reference data on the murine cardiovascular anatomy and physiology are lacking. In this work, we developed and validated an *in silico*, one dimensional model of the murine systemic arterial tree consisting of 85 arterial segments. Detailed aortic dimensions were obtained *in vivo* from contrast-enhanced micro-computed tomography in 3 male, C57BL/6J anesthetized mice and 3 male ApoE$^{-/-}$ mice, all 12-weeks old. Physiological input data were gathered from a wide range of literature data. The integrated form of the Navier-Stokes equations was solved numerically to yield pressures and flows throughout the arterial network. The resulting model predictions have been validated against invasive pressure waveforms and non-invasive velocity and diameter waveforms that were measured *in vivo* on an independent set of 47 mice. In conclusion, we present a validated one-dimensional model of the anesthetized murine cardiovascular system that can serve as a versatile tool in the field of preclinical cardiovascular research.

Keywords: high-frequency ultrasound, contrast-enhanced micro-CT, 1D mouse model, systemic arterial tree, ventricular-vascular coupling

1 Introduction

Cardiovascular disease is often studied in a preclinical setting since small animal models offer more flexibility, easier access to *in* and *ex vivo* tissues, and faster disease progression than humans. Mice in particular are a common model in hypothesis-driven cardiovascular research (Treuting et al., 2012) due to their short lifespan, their small size, the similarity of their well-decrypted genome with the human one and, most importantly, the possibility to induce genetic modifications (Pennacchio, 2003). Genetically or pharmacologically altered mouse models have provided insight into (amongst many other cardiovascular applications) abdominal aortic aneurysm (Trachet et al., 2014a,b), stable and unstable atherosclerotic plaque (Van der Donckt et al., 2014; De Wilde et al., 2015), diabetes (Reed and Herold, 2015), hypertrophy (Yamaguchi et al., 2007) and Marfan syndrome (Campens et al., 2015). However, since mice have a much smaller (aortic dimensions are 10x smaller, Tab. 1) and faster (average, non-anesthetized heart rate is 10x higher) cardiovascular system, the interpretation of these results requires a cautious translation between murine and human sys-

tems. Striking similarities between human and murine aortic flow velocity and pressure waveforms (Nichols et al., 2011), as well as a highly similar branching pattern of the aortic arch (Casteleyn et al., 2010), have been reported in literature. However, in-depth research on aortic anatomy and physiology is not straightforward since, both in humans and mice, (non-)invasive measurements are (i) technically difficult to obtain, (ii) limited to a restricted number of aortic locations, and (iii) need to be justified from an ethical perspective. In a human setting, these limitations can be circumvented since reference data for both anatomy and physiology are readily available for many arterial locations. The development of a wide range of 1D models of the human arterial circulation (Avolio, 1980; Bessems et al., 2007; Mynard and Smolich, 2015; Sherwin et al., 2003; Stergiopulos et al., 1992; Wemple and Mockros, 1972) has allowed researchers to study the effect of alterations in anatomy or physiology (Vardoulis et al., 2011) without the ethical and technical limitations of *in vivo* measurements. In mice, the available data are focused on arterial physiology rather than anatomy. To the best of our knowledge, the most complete computational model of the murine arterial tree is the FSI model of Cuomo et al. (2015).

Tab. 1: Arterial tree segments and dimensions

Arterial segment name	Arterial segment number (right/left)	Length, mm	Proximal lumen diameter, mm	Distal lumen diameter, mm	Distensibility, 10^{-3} 1/mmHg	Terminal resistance, mmHg·s·ml^{-1}	Terminal compliance, 10^{-8} ml/mmHg
Ascending aorta	1	2.6	1.41	1.54	2.95		
Aortic arch A	2	0.7	1.33	1.33	2.79		
Brachiocephalic trunk	3	2.1	0.80	0.71	1.97		
Right common carotid	4	10.2	0.52	0.49	1.52		
Right external carotid	5	2.6	0.42	0.36	1.27		
Right internal carotid	6	1.8	0.41	0.39	1.42		
Right subclavian A	7	1.2	0.55	0.53	1.68		
Right vertebral	8	13.3	0.40	0.27	1.13		
Right axillary	9	7.8	0.35	0.27	1.11	1,015.7	9.8
Costocervical trunk	10	2.7	0.26	0.23	0.93	4,962.3	6.0
Internal mammary	11	5.1	0.25	0.23	0.93	2,198.4	6.0
Left common carotid	12	13.3	0.63	0.52	1.55		
Left internal carotid	13	1.8	0.44	0.41	1.43		
Left external carotid	14	2.6	0.43	0.40	1.27		
Aortic arch B	15	1.2	1.20	1.18	2.58		
Left subclavian A	16	1.8	0.61	0.55	1.58		
Left vertebral	17	13.2	0.34	0.26	1.12		
Left subclavian B	18	6.1	0.40	0.32	1.36		
Left axillary	19	3.0	0.25	0.22	0.92	2,079.2	5.5
Left cervical trunk	20	2.4	0.32	0.30	1.10	948.1	11.9
Thoracic aorta A	21	12.2	1.16	1.11	2.45		
Intercostals	22	1.6	0.51	0.51	1.42	592.8	973.3
Thoracic aorta B	23	12.2	1.11	1.07	2.39		
Left suprarenal	24	3.0	0.33	0.31	1.04	4,414.0	133.3
Thoracic aorta C	25	2.3	1.06	1.06	2.34		
Coeliac	26	3.1	0.46	0.43	1.32		
Hepatic	27	3.4	0.24	0.24	0.86	2,955.8	66.7
Lieno-gastric	28	5.1	0.31	0.27	0.98	1,680.4	110.0
Lieno-pancreatic	29	6.9	0.29	0.27	0.96	1,777.2	124.3
Abdominal aorta A	30	1.8	1.00	0.97	2.26		
Superior mesenteric	31	4.7	0.60	0.56	1.56		
Ileocolic	32	1.3	0.31	0.24	0.94	2,439.5	674.1
Ileac and jejunal branches	33	2.6	0.55	0.53	1.48	319.3	1,099.6
Abdominal aorta B	34	0.4	0.93	0.93	2.14		
Right renal	35	2.9	0.51	0.49	1.40	641.3	666.6

Arterial segment name	Arterial segment number (right/left)	Length, mm	Proximal lumen diameter, mm	Distal lumen diameter, mm	Distensibility, 10⁻³ 1/mmHg	Terminal resistance, mmHg·s·ml⁻¹	Terminal compliance, 10⁻⁸ ml/mmHg
Abdominal aorta C	36	1.9	0.88	0.87	2.06		
Right spermatic artery	37	5.1	0.26	0.23	0.87	21,346.7	4.3
Abdominal aorta D	38	1.2	0.85	0.83	2.00		
Left renal	39	1.5	0.47	0.45	1.33	862.3	400.0
Abdominal aorta E	40	1.0	0.80	0.80	1.94		
Left spermatic artery	41	5.3	0.23	0.22	0.83	46,939.9	3.9
Abdominal aorta F	42	9.0	0.78	0.70	1.85		
Middle caudal	43	28.1	0.34	0.22	0.96	20,303.3	4.5
Abdominal aorta G	44	0.7	0.70	0.70	1.77		
Common iliac	45/46	3.4	0.51	0.47	1.41/1.41		
Inner iliac	47/53	4.0	0.23	0.18	0.77/0.77	37,180.5	2.4
External iliac	48/54	1.5	0.48	0.47	1.36/1.36		
Pudic-epigastric trunk	49/55	1.3	0.27	0.23	0.88/0.88	20,430.5	4.6
Femoral	50/56	8.6	0.47	0.43	1.32/1.32		
Posterior tibial	51/57	4.3	0.30	0.23	0.98/0.98	6,807.5	6.0
Anterior tibial	52/58	3.0	0.35	0.26	0.98/0.98	6,761.8	5.8
Right subclavian B	59	0.7	0.53	0.53	1.62		
Maxillary	60/84	8.3	0.26	0.20	1.23/1.24	2,373.8/ 1,797.9	31.4/32.3
Ophthalmic	61/82	3.2	0.33	0.21	1.13/1.22	3,203.2/ 1,988.3	16.5/22.4
Internal carotid sinus	62/81	4.8	0.35	0.30	1.36/1.37		
Anterior choroidal	63/80	1.3	0.19	0.14	0.78/0.83	10,443.2/ 8,857.9	5.6/7.4
ICA distal	64/79	1.5	0.28	0.25	1.12/1.20		
Posterior cerebral C	65/71	2.7	0.22	0.20	0.84/0.90		
Posterior cerebral B	66/70	3.5	0.22	0.18	2.00/1.83	839.5/898.5	249.4/173.6
Posterior cerebral A	67/68	2.6	0.19	0.17	1.01/1.01		
Basilar artery	69	4.8	0.23	0.24	1.33		
Middle cerebral	72/78	2.2	0.19	0.16	0.86/1.82	6,068.4/ 4,812.6	57.9
Anterior cerebral	73/77	2.6	0.24	0.21	1.00/2.07		
Supraorbital	74	2.1	0.31	0.23	2.00		
Naso-frontal	75	2.0	0.19	0.16	1.59	2,427.7	95.1
Anterior facial	76	3.2	0.18	0.13	1.47	3,464.2	58.9
fac. occ. left sup. thy. asc. ph. lyng. fac.	83/85	3.2	0.19	0.16	1.05/1.04	3,865.4/ 5,087.7	16.8/16.3

They set up a 3D model to investigate the effect of invasive pressure measurements on local hemodynamics, while accounting for ventricular-vascular coupling. However, their 3D model was based on a single mouse and only included the major branches. An extensive description of the 'reference' murine arterial anatomy and physiology has, to the best of our knowledge, never been reported and a validated *in silico* model describing the average murine systemic tree and its hemodynamics is lacking. A validated numerical model of the murine circulation could facilitate the implementation of the 3R's principle (Refine, Reduce, Replace) in small animal research and contribute to minimize the use of animals by providing valuable insight into murine hemodynamics without animal suffering.

In this work, we used high-resolution, contrast-enhanced micro-CT to obtain reference data on the *in vivo* anatomy of the entire systemic arterial tree in mice. We subsequently combined these measurements with a wide range of literature data to translate an existing one-dimensional model of the human systemic arterial tree (Reymond et al., 2009) into a murine setting. The resulting *in silico* model of the anesthetized murine systemic arterial tree includes 85 arterial segments and predicts pressure and velocity waveforms at all arterial locations without the need for arduous invasive measurements. We demonstrated the validity of the model by comparing its predicted pressure, velocity and diameter waveforms to those measured *in vivo* in a large sample of young, male laboratory mice.

2 Animals, materials and methods

2.1 *In vivo* measurements
Mice
All procedures were approved by the Ethical Committee of Canton Vaud, Switzerland (EC 2647.1 for the wild type mice, EC 2647.2 for the apolipoprotein E gene-deleted [ApoE$^{-/-}$] mice) and performed according to the guidelines from Directive 2010/63/EU of the European Parliament on the protection of animals used for scientific purposes. Male wild type C57BL6/J and male ApoE$^{-/-}$ mice on a C57BL6/J background were purchased from Janvier (Saint-Berthevin, France). All surgery and measurements were performed under isoflurane anesthesia, and all efforts were made to minimize suffering. The 3R (refine, reduce, replace) principle was applied to minimize the number of laboratory animals. Initial micro-CT, invasive pressure and ultrasound measurements were performed on five wild type, male C57BL/6J mice, 12-15 weeks old, that served as control animals in a study on murine abdominal aortic aneurysms (AAA) (Trachet et al., 2014b). Subsequent micro-CT (n = 3) and ultrasound (n = 47) measurements were performed on male ApoE$^{-/-}$ mice on a C57BL/6J background, 12 weeks old, that served as baseline data in a follow-up study on murine AAA (Trachet et al., 2015). Mice were housed in the controlled environment of the EPFL animal facility, which is a part of the Lemanic animal facility network, and had *ad libitum* access to water and food (standard rodent chow). The overall well-being of the animals was inspected twice per day. Both wild type and ApoE$^{-/-}$ mice were euthanized at humane endpoints defined by their respective studies (just after micro-CT for wild types, after 10, 18 or 28 days of angiotensin II-infusion for ApoE$^{-/-}$ mice).

Contrast-enhanced micro-CT
Animals were anesthetized by inhalation of 1.5% isoflurane and injected intravenously in the lateral tail vein with 100 μl/25 g body weight of Exitron (Miltenyi Biotec, Germany). The animals were subsequently scanned *in vivo* in dorsal recumbency with a Quantum FX micro-CT scanner (Caliper Life Sciences, Hopkinton, Massachusetts), which has been optimized for longitudinal studies owing to its low radiation dose. Acquisition was performed with a 90 kVp tube voltage and a current of 160 μA. Each animal underwent 5 consecutive scans, with region of interest focused on the head, thorax, abdomen, legs and tail, respectively. Each scan lasted for 2 minutes, and images were obtained with a 24 mm transverse field of view and a theoretical spatial pixel size of 50 μm. Micro-CT images were reconstructed using an in-house method based on the iterative maximum-likelihood polychromatic algorithm (De Man et al., 2001).

Invasive pressure
In five wild type mice, a 1.2 F Scisense catheter (Transonic, Maastricht, The Netherlands) with two pressure sensors spaced 2 cm apart was inserted via an incision in the femoral artery. The catheter was guided into the correct position using simultaneous long axis BMode ultrasound, and allowed to settle for 10 minutes. Continuous pressure waveforms were recorded with the tip of the catheter (i.e., the first pressure sensor) at the descending, thoracic and abdominal aorta.

High-frequency ultrasound
Ultrasound imaging was performed with a high-frequency ultrasound device (Vevo 2100, VisualSonics, Toronto, Canada). During the procedure animals were anesthetized by inhalation of 1.5% isoflurane and fixed on the imaging table in dorsal position. Physiological function (respiration and heart rate obtained from ECG) was monitored while the animal was positioned on the heated handling table. All measurements were performed by a single, experienced operator. In 5 wild type mice and 47 ApoE$^{-/-}$ mice, pulsed Doppler measurements were obtained in the ascending, descending, and 5 locations along the thoraco-abdominal aorta: the thoracic aorta, the supraceliac region just cranial to the bifurcation of the celiac artery, the paravisceral region cranial to the trifurcation of the mesenteric and right renal arteries, the pararenal region caudal to the trifurcation of the mesenteric and right renal arteries and the infrarenal region caudal to the bifurcation of the left renal artery. Pulsed Doppler measurements were also obtained in the celiac, mesenteric and renal (left and right) arteries. In the 5 wild type mice additional pulsed Doppler measurements were obtained prior to pressure probe insertion in the brachiocephalic trunk, common, internal and external carotid arteries (left and right), caudal and iliac arteries.

Ultrasound Pulsed Doppler waveforms were traced within a custom-made environment in Matlab. For each measurement location, the average of three different waveforms was calculated. The resulting waveform vectors were subsampled to

501 points and filtered using a Savitsky-Golay filter of an order 3 and window width 51. All blood flow velocity ultrasound measurements were divided by a factor of 2, assuming that the ultrasound velocity measurements correspond to the maximum centerline velocity of a parabolic velocity profile (Reddy et al., 2003).

In wild type mice RF (radio frequency) diameter waveforms were obtained with long axis MMode imaging at the same locations as invasive pressure measurements, while in ApoE$^{-/-}$ mice RF diameter waveforms were measured with MMode at the ascending aorta and at 2 locations in the abdominal aorta (cranial to the celiac and caudal to the left renal artery). A custom-written platform in Matlab, based on the algorithm described by Rabben et al. (2002), was used to reconstruct the complete

Fig. 1: Schematic representation of arterial tree
A: main systemic arterial tree, B: cerebral vasculature, connected via the carotids (segments 4, 12) and the vertebrals (segments 8, 17) to the main arterial tree shown in A, C: detail of the heart, ascending aorta and carotid branches, D: detail of the principal abdominal aortic branches. R: right; L: left.

MMode image from RF data as described in previous work (Trachet et al., 2015). For each measurement, 3 cardiac cycles were subsequently selected and plotted as a reference for semi-automatic wall segmentation guided by the user. The tracked aortic wall movement yielded highly accurate *in vivo* diameter waveforms (Fig. 4).
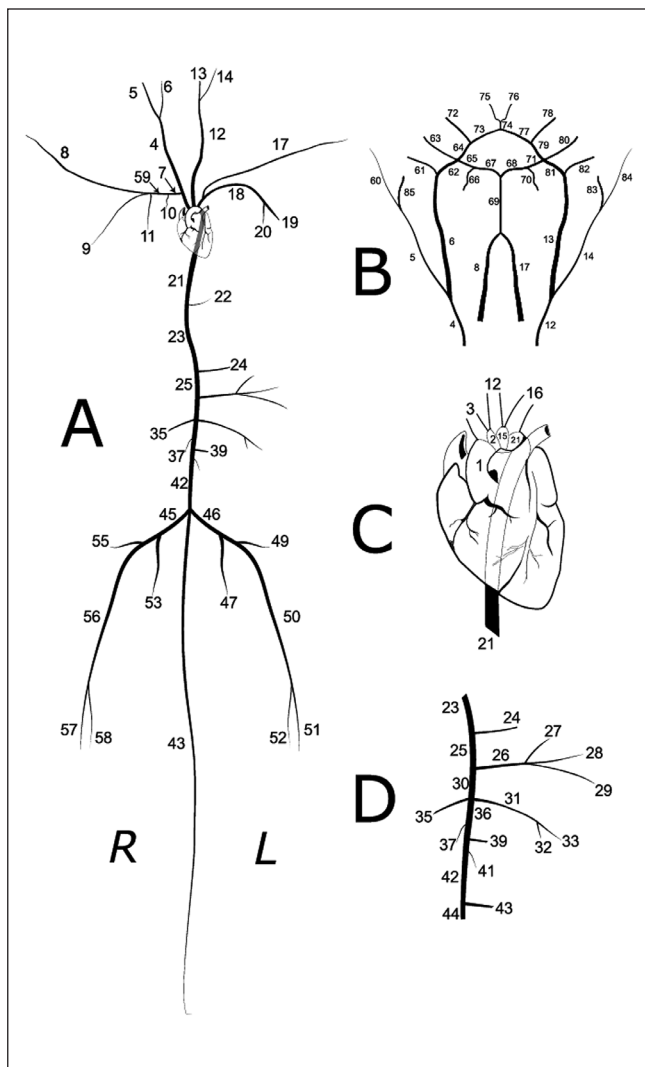
2.2 *In silico* model

For an in-depth description of the governing equations and assumptions that were made in the modeling approach, we refer to a previous manuscript describing the human model (Reymond et al., 2009). Here, a synopsis of the most important modeling assumptions is given, with emphasis on the aspects in which the murine modeling assumptions differ from the human ones.

Arterial tree
As literature data on murine anatomy are scarce and restricted to the main aorta, we based the arterial tree only on dedicated *in vivo* measurements. For n = 3 C57BL/6J mice, reconstructed micro-CT images were converted into TIFF format and imported into the 3D segmentation software package Mimics (Materialise, Leuven, Belgium). Arterial branches were segmented when micro-CT resolution allowed so, and when their inclusion was judged physiologically relevant for future applications. This resulted in an averaged tree consisting of 85 segments (Tab. 1). For each segment, inlet and outlet areas were measured perpendicular to and segment length was measured along the centerline that was calculated in Mimics. To account for variation due to differences in genetic background, the detailed data from 3 wild type mice were complemented with diameters and lengths of the main aorta and its major branches (carotids, celiac, mesenteric and renal arteries) from micro-CT scans of the thorax and abdomen in 3 ApoE$^{-/-}$ mice. The schematic representation of the resulting arterial tree is shown in Figure 1. The 8 pairs of intercostal arteries were accounted for by introducing a single vessel with a blood flow equivalent of the set of the 8 intercostal pairs, similar to what was done in the human model (Reymond et al., 2009).

Governing equations
The murine systemic arteries were modeled as compliant tapering cylindrical vessels with a viscoelastic wall. The 1-D formulation of the continuity equation and the incompressible, axisymmetric Navier-Stokes equations for a Newtonian fluid governed the propagation of blood flow and pressure in the model (while taking into account the Fåhræus-Lindqvist effect on viscosity, see below). A third, constitutive equation was used to relate the distending pressure to the local cross-sectional area, thus describing the viscoelastic properties of the arterial wall. The system of three equations with three unknowns (pressure, flow and area) was solved numerically with an implicit finite difference scheme over 8 cardiac cycles, using an in-house MATLAB code previously developed for the human arterial tree (Reymond et al., 2009). The Witzig Womersley theory was implemented to approximate the pulsatile effects on the velocity profile, which was needed to calculate convective acceleration and wall shear stresses in the momentum equation.

Viscoelastic modeling of the wall

Holenstein's model (Holenstein et al., 1980) was implemented to describe the viscoelastic wall behavior. The instantaneous lumen area under a distending pressure P was expressed as the sum of a nonlinear elastic and a viscoelastic component:

$$A(t) = A^e[P(t)] + A^v(t)$$

The elastic component of the local area, Ae relates to the distending pressure by its elastic compliance, C_A^e. To account for both pressure and location dependence, we assumed that elastic area compliance was the product of a pressure-dependent function, termed $C_p^e(P)$, and a location-dependent function, termed $C_d^e(\bar{d}, P_{ref})$. As Langewouters (Langewouters, 1982, 1984) proposed for the pressure dependency of the static compliance:

$$C_p^e(P) = \frac{C_m}{1 + \left[\frac{P - P_{maxC}}{P_{width}}\right]^2}$$

Fitting of the parameters was based on literature (Le et al., 2011) as well as in house pressure-diameter measurements on excised C57BL/6 murine aortas, which resulted in the following values: $C_m = 17.3$ m²/mmHg, $P_{maxC} = 27.2$ mmHg and $P_{width} = 20$ mmHg. The local diameter-dependent variation of the elastic area compliance was derived from the following equation:

$$C_d^e(\bar{d}, P_{ref}) = \frac{A}{\rho PWV^2(\bar{d}, P_{ref})}$$

In order to model the location-dependent compliance, local aortic stiffness data were gathered from a wide range of literature data (Agianniotis and Stergiopulos, 2012; Bolduc et al., 2012;
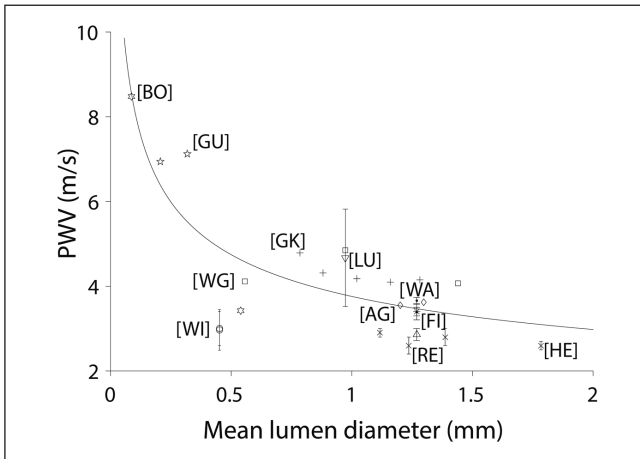
Fig. 2: Pulse wave velocity (PWV) values reported in literature for different arterial sites as a function of lumen diameter
Acronyms refer to the publication reporting the values Acronyms refer to the publication reporting the values (AG: Agianniotis and Stergiopulos, 2012; BO: Bolduc et al., 2012; FI: Fitch et al., 2006; GK: Guo and Kassab, 2003; GU: Guo et al., 2006; HE: Herold et al., 2009; LU: Luo et al., 2009; RE: Reddy et al., 2003; WI: Williams et al., 2007; WA: Wang, 2005; WG: Wagenseil et al., 2005). Standard deviations are shown where available.

Fitch et al., 2006; Guo and Kassab, 2003; Guo et al., 2006; Herold et al., 2009; Luo et al., 2009; Reddy et al., 2003; Wagenseil et al., 2005; Wang, 2005; Williams et al., 2007). If local *ex vivo* pressure-diameter curves or distensibility values were reported, these were converted into local pulse wave velocities (PWV) using the Bramwell-Hill equation. To allow for comparison with the human model, PWV values were subsequently plotted against lumen area (Fig. 2). In spite of some well anticipated dispersion, we found an inverse relation between artery size and PWV:

$$PWV(\bar{d}) \approx \frac{a}{\bar{d}^b}$$

The coefficients obtained for the best fit (PWV in m/s, diameter in m) were α = 0.3693 and b = 0.3359, with R² = 0.6, which is a better fit than what was obtained in the human model (Reymond et al., 2009).

The viscoelastic area component, $A^v(t)$, was calculated by the convolution product between the elastic area, A^e, and the derivative of a creep function, J(t):

$$A^v(t) = \int_0^\infty j(\tau) A^e[P(t-\tau)]d\tau$$

$$j(\tau) = \tilde{\alpha}\frac{e^{-t/\tau 2} - e^{-t/\tau 1}}{t}$$

Measurements on visco-elastic properties of mouse arterial tissues were kindly provided by Tian et al. (2013), but as there was much scattering in the data we did not manage to obtain a physiologically reasonable fit. Following Reymond et al. (2009), we used Holenstein's fitted values for τ1 (0.00081s) and τ2 (0.41s), which had been fit on canine data from Bergel (1961). Further, we assumed that the viscoelastic coefficient α̂ increases linearly from the heart to the distal beds:

$$a \cong a_1 \cdot \bar{d} + b_1$$

Since the dimensions of the human brain vasculature (0.5-4 mm) are approximately of the same order of magnitude as the murine systemic arteries (0.13 to 1.54 mm), we decided to apply the fit obtained for the human brain vasculature in the murine systemic arteries. This resulted in values of $a_1 = -0.0062$ mm⁻¹ and $b_1 = 0.34$.

Fåhræus-Lindqvist effect

The Fåhræus-Lindqvist effect describes a significant decrease of apparent blood viscosity in tubes of diameters less than 300 μm (Fahraeus and Lindqvist, 1930) and down to approximately 10 μm (Sugihara-Seki and Fu, 2005). In the murine anatomy obtained for our model, 26 arterial segments out of 85 were of a diameter below the critical 300 μm. We therefore implemented an empirical relationship to account for the dependence of relative apparent viscosity on tube diameter and hematocrit, based on *in vitro* and *in vivo* observations, for a hematocrit equal to 45% (Secomb and Pries, 2013).

*Distal vasculature model and boundary conditions
at terminal vessels*
A three-element windkessel model was used to account for the cumulative resistance and compliance of all vessels distal to the terminal segments. Following Reymond et al. (2009), the windkessel compliance C_T^i was assumed to be proportional to the area compliance C_A^i of the terminal vessel at its distal end:

$$c_T^i \cong c_T \frac{c_A^i}{\sum c_A^i}$$

where $C_T = \sum_i C_T^i$ is the part of the total volume compliance attributed to peripheral vessels beyond the termination sites.

The addition of the segments' volume compliance and the compliance of the peripheral beds yielded the total systemic vascular compliance:

$$c_v = \sum_n^i c_{v,i} + \sum_m^i c_{T,i}$$

where n = 85 is the total number of arterial segments and m = 39 is the total number of terminal beds. The volume compliance for each segment was calculated by integrating the area compliance over the segment length. Volume compliances (and, in order to preserve consistency, distensibilities) were adjusted to match the literature value of 2.67 x 10^{-4} ml/mmHg for the compliance of the murine central aorta including some of its major branches (Guo and Kassab, 2003).

For the estimation of the total terminal compliances, we followed the assumption that 20% of the total systemic compliance lies in the terminal beds (Reymond et al., 2009; Stergiopulos et al., 1992). Terminal resistances were calculated based on flow rates into major branches that were reported by Trachet et al. (2011). At locations where no experimental data were available, we completed the values assuming that the mean wall shear stress (given by Poiseuille's law) was the same as for nearby arteries. Unlike the human model, where the entire mean pressure drop was assumed to occur in the distal beds, we accounted for losses within the system by subtracting the pressure drop predicted by Poiseuille's law prior to calculating the terminal resistances.

Arterial bifurcations
Continuity of pressure and flow were imposed across each branching point. To minimize forward wave reflections, the characteristic impedances of all segments were adapted so that the absolute value of the reflection coefficient was <0.1 at all bifurcations.

Heart model
At its proximal end, the arterial tree was coupled to a varying elastance model of the left ventricle (Sagawa, 1981). Following the argumentation of Reymond et al. (2009), we imposed the following expression for the varying elastance of an ejecting heart:

$$E(t) = E^*(t)[1 - kQ(t)]$$

where E^* represents the elastance that would be measured during an isovolumic (non-ejecting) contraction, and k a con-

stant relating the internal resistance of the left ventricle to the ventricular pressure during an isovolumic contraction. We derived the isovolumic elastance E^* from the global normalized elastance curve reported by Senzaki et al. (1996), given the striking similarity in normalized elastance curves between humans and mice (Georgakopoulos et al., 1998). This required the use of a "standard" aortic flow waveform, which we obtained from averaged flow velocity and aortic diameter waveforms at the ascending aorta in 47 ApoE$^{-/-}$ mice. The value of k was derived iteratively, by minimizing the difference between the elastance resulting from the 1-D model and the original one from Senzaki et al. (1996). The final k-value was 0.42 s/ml. Other parameter values for the heart model were obtained from literature and, where needed, calculated from reported P-V loops. Due to the large variety of measurement methods for mice of different strains under different anesthesia methods, the mean literature values of minimum (Cingolani and Kass, 2011; Georgakopoulos et al., 1998; Pacher et al., 2008; Shioura et al., 2007; Yang et al., 1999) and maximum (Cingolani and Kass, 2011; Lips et al., 2004; Nemoto et al., 2002; Pacher et al., 2008; Shioura et al., 2007) elastance as well as dead volume (Cingolani and Kass, 2011; Georgakopoulos et al., 1998; Grieve et al., 2004) were subsequently tuned to yield a physiological pulse pressure and velocity waveform at the proximal aorta. The final values were 0.1 μl for the dead volume, 0.09 mmHg/μl for the minimum elastance and 6.2 mmHg/μl for the maximum elastance. End-diastolic pressure was taken equal to the mean of the literature values (Cingolani and Kass, 2011; Grupp et al., 1993; Pacher et al., 2008; Shioura et al., 2007; Yang et al., 1999), which was 4.6 mmHg. Given the lack of reports on venous resistance values for mice, we decided on a value of 0.23 mmHg·s·ml^{-1}, which yielded physiological heart parameters (presented in the results section). Anesthetized heart rate was set equal to 445 bpm, i.e., the average of the measured heart rate values (during ultrasound acquisition) of the 47 ApoE$^{-/-}$, and was close to the mean heart rate of 480 bpm of several literature reports (Cingolani and Kass, 2011; Grupp et al., 1993; Pacher et al., 2008; Shioura et al., 2007; Yang et al., 1999). The time to maximum elastance was set equal to 59 ms for a heart cycle of 0.135 s.

Lumped parameter windkessel model
Global arterial properties can be estimated by coupling the time-varying elastance heart model to a lumped parameter windkessel model representing the whole arterial tree (Segers et al., 2000, 2002; Stergiopulos et al., 1999; Westerhof et al., 2009). For an overall validation for the model, we coupled the heart model to a four-element windkessel model so as to compare the arterial model parameters of total systemic resistance, total compliance and aortic characteristic impedance to values reported by Segers et al. (2005).

Cerebral circulation
The carotid arteries are expected to be susceptible to returning waves from the highly resistant cerebral sites (Reymond et al., 2009). We therefore investigated the effect of the presence of the cerebral vasculature on the blood flow and pressure estimates in the right carotid artery. In order to ensure a fair comparison, the

distal sites of the carotids and vertebral arteries were terminated with lumped three-element WK models appropriately tuned to account for the same total terminal resistance and compliance as with the presence of the brain model.

Pressure in the tail
The mouse tail is a specific region of interest, since tail-cuff pressure measurements are the most common noninvasive method to determine arterial blood pressure in mice. Yet, thermoregulatory vasomotion in the tail of the mouse can cause a significant variance in tail blood flow (Gordon, 1993) and, hence, in tail-cuff pressure measurements (Hoyt et al., 2007). The modeled percentage of proximal aortic blood flow to the caudal artery was 3%. In order to simulate different thermoregulatory states, a parameter study was performed in which the blood flow to the caudal artery was varied between 1% and 5% of the proximal aortic blood flow.

3 Results

3.1 General physiological parameters
Main hemodynamic parameters estimated from the 1D model are presented in Table 3, along with values of the 3D model published by Cuomo et al. (2015). Cardiac output was 14 ml/min, stroke volume was 31.4 μl, heart ejection fraction was 61% and mean blood pressure in the proximal aorta was 98 mmHg. The aortic PWV was calculated with the transit time method between the proximal ascending aorta and the distal abdominal aorta just before the iliac bifurcation and was found equal to 4.44 m/s. In the proximal aorta, systolic pressure was 121 mmHg and diastolic pressure was 79 mmHg, with the mean flow equal to 0.23 ml/s. Modeling of the entire

murine arterial tree with the four-element lumped parameter windkessel model yielded the parameters reported in Table 3. Maximum values of Womersley and Reynolds numbers within the murine circulation were 2.5 and 175, respectively.

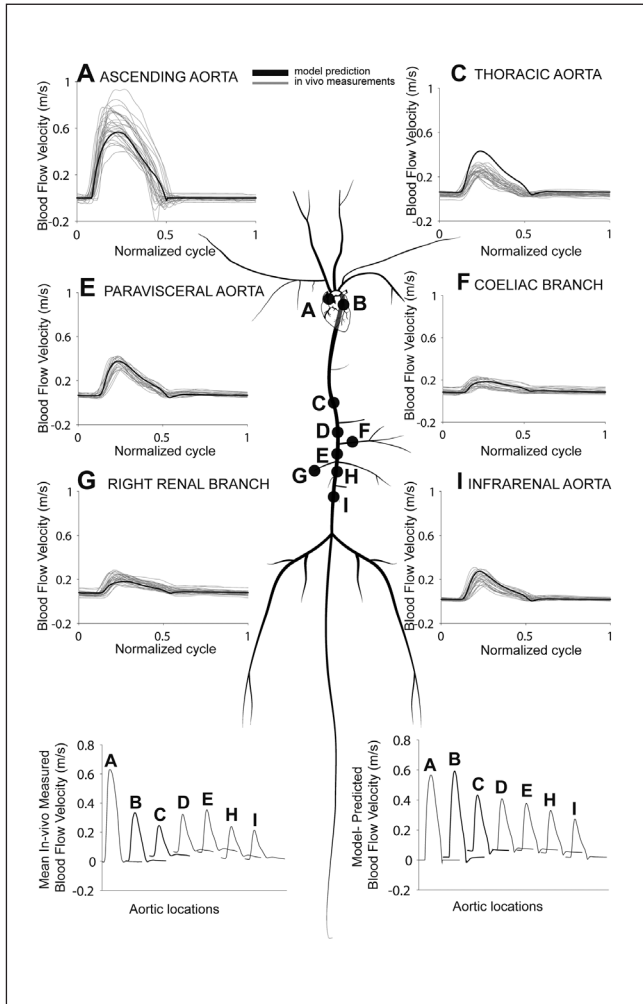### 3.2 Model predictions vs *in vivo* measurements
Model predictions of blood flow velocity, mean blood pressure and pulse pressure as well as the mean value of the validation set of 47 *in vivo* measurements are summarized for all major arterial sites in Table 2.

Figure 3 displays the modeled blood flow velocity waveforms against *in vivo* measurements performed on a set of 47 ApoE^{-/-} mice at 6 sites along the arterial tree. Due to the great variability in heart rate among different measurements, the duration of the cardiac cycle has been normalized to allow for comparison between different measurements and the model prediction. The bottom panel of Figure 3 shows the model blood flow velocity waveforms along the aorta, starting from the proximal ascending aorta and ending in the infrarenal aortic part, before the iliac bifurcation. The mean waveform of *in vivo* velocity measurements performed on the same aortic locations is also displayed separately in the bottom panel. A good overall agreement in amplitude and waveform can be noted. The only arterial sites where the model prediction presents a similar waveform but different amplitude from the *in vivo* measurements are the descending and thoracic aorta.

In Figure 4, the modeled diameter and pressure waveforms are compared with the corresponding *in vivo* measurements. Similar to the flow velocity waveforms of Figure 3, the heart cycle duration has been normalized in order to facilitate the comparison between the diameter waveforms. The mean pressure of the model prediction falls within the range of the measured pressure waveforms at all locations, yet the lat-

Tab. 2: Quantification of pressure and blood flow velocity model predictions and corresponding *in vivo* measurements at different locations along the aortic tree
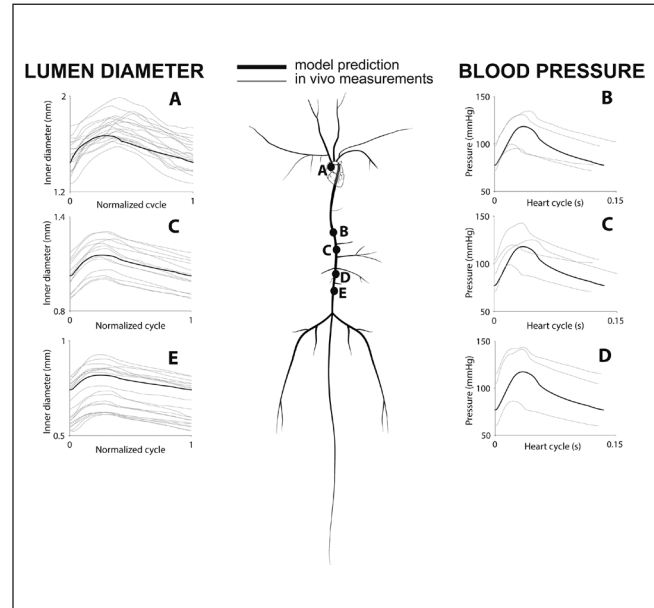Values are means ± SD.

	Blood flow velocity (m/s)		Mean pressure (mmHg)	
	In vivo measurements	Model	*In vivo* measurements	Model
Ascending aorta	0.17 ± 0.24	0.15	NA	98.2
Descending aorta	0.09 ± 0.12	0.15	96.5 ± 18.6	97.3
Thoracic aorta	0.09 ± 0.07	0.15	99.6 ± 17.4	95.5
Supraceliac region	0.12 ± 0.08	0.15	104.9 ± 16.2	95.2
Coeliac artery	0.12 ± 0.03	0.11	NA	94.4
Paravisceral region	0.13 ± 0.08	0.13	NA	94.9
Mesenteric artery	0.13 ± 0.05	0.13	NA	94.2
Right renal	0.11 ± 0.04	0.11	NA	94.2
Pararenal region	0.08 ± 0.07	0.11	107.2 ± 31.4	94.6
Left renal	0.10 ± 0.04	0.09	NA	94.0
Infrarenal aortic region	0.06 ± 0.06	0.07	NA	94.1

Fig. 3: Model flow velocity predictions against *in vivo* flow velocity measurements over a normalized timescale at six locations along the arterial tree
The bottom panel depicts model flow velocity predictions at 7 aortic locations extending from proximal to distal abdominal aorta and the mean flow velocity waveform of the *in vivo* measurements performed on the same locations. A: ascending aorta, B: descending aorta, C: thoracic aorta, D: supraceliac aorta, E: paravisceral region, F: coeliac branch, G: right renal branch, H: I: infrarenal aorta.

Fig. 4: *In vivo* pressure and diameter measurements compared to model results at different aortic sites
The left panels show the model prediction of inner lumen diameter change over a normalized cardiac cycle against ultrasound MMode measurements performed at locations A, C and E.
The right panels show the modeled prediction of aortic pressure over a normalized cardiac cycle against invasive pressure measurements at sites B, C and D.
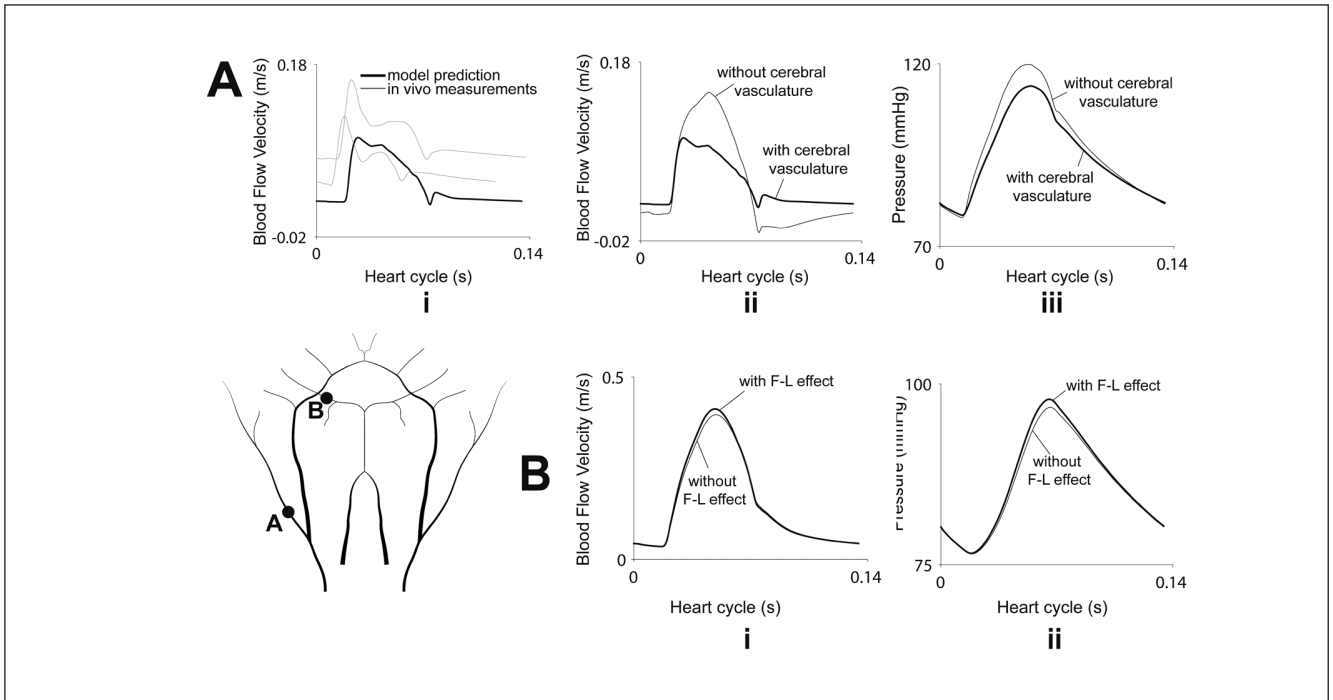A: ascending, B: thoracic, C: supraceliac region, D: pararenal region, E: infrarenal region.

3.3 Parameter studies

Figure 5a displays the effect of inclusion of the brain vasculature on the model flow velocity and pressure waveform prediction in the right external carotid artery. In the first panel (i) the modeled flow velocity waveform compares relatively well to *in vivo* measurements performed in the right external carotid artery. Middle (ii) and right (iii) panels show that considerable differences occur in the carotid flow and pressure waveforms with and without inclusion of the cerebral vasculature into the model. In the absence of the cerebral tree, there is non-physiological backflow and a substantially altered waveform.

Figure 5b shows the Fåhræus-Lindqvist effect in the posterior cerebral segment, which has a mean diameter equal to 220 μm. Inclusion of the Fåhræus-Lindqvist effect into the model results in a 0.6% decrease in mean pressure and a 2.1% decrease in mean flow velocity at this location.

The effect of the Witzig-Womersley formulation for wall shear stress and convective acceleration is small on predicted pressure and flow: in the common iliac artery, use of the Witzig-Womersley formulation leads to a 0.1% decrease in the mean pressure and marks no change in the mean flow rate prediction, while in the thoracic artery it leads to a 0.1% decrease in mean pressure and a 0.2% decrease in mean flow rate.

When the inflow rate at the tail was reduced from 3% to 1%, central pressure slightly increased from 98 to 99 mmHg, while

ter suffer from high inter-subject variability (cf. Tab. 2). The modeled pulse pressure is 41.7 mmHg in the ascending aorta and drops to 40.2 mmHg in the infrarenal aorta. The *in vivo* diameter waveforms are similar in shape to the *in vivo* pressure waveforms (e.g., panel C). The modelled inner lumen diameter change from diastole to systole (Δd) in the ascending aorta is 0.22 mm, whereas in the supraceliac aortic region it is 0.13 mm and 0.08 in the infrarenal aortic region. This corresponds very well to the *in vivo* diameter measurements which yielded mean Δd values of 0.23 ± 0.07 mm in the ascending aorta, 0.15 ± 0.03 mm in the supraceliac aortic region and 0.09 ± 0.02 in the infrarenal part of the aorta.

Fig. 5: Influence of cerebral vasculature on model predictions

A. Influence of cerebral vasculature on model predictions in the right external carotid artery: i) model flow velocity prediction against *in vivo* velocity measurements in the same location, ii) Effect of brain vasculature omission on blood flow velocity waveform, iii) Effect of brain vasculature omission on pressure waveform. B. Fåhræus-Lindqvist (F-L) effect on blood flow velocity and pressure waveform in posterior cerebral C segment.

the mean blood pressure in the tail increased from 83 mmHg to 90 mmHg. In this case, the systolic and diastolic blood pressure in the tail were 109 mmHg and 74 mmHg, respectively. When the flow in the caudal artery was increased to 5%, central pressure slightly decreased to 97 mmHg, while the mean blood pressure in the tail dropped to 77 mmHg. The systolic and diastolic blood pressure in the tail decreased to 93 mmHg and 64 mmHg, respectively.

4 Discussion

The original 1D model of the human systemic arterial tree that formed the basis of this work was developed (Stergiopulos et al., 1992) and improved (Reymond et al., 2009) in our lab, and has been successfully used as a research tool in a number of subsequent studies (Vardoulis et al., 2011, 2012). Due to the fact that it includes a heart model, ventricular-vascular coupling, a detailed description of the cerebral circulation, and a detailed description of shear stress and wall viscoelasticity, the original model can be considered the most complete model available in literature. The effect of separate features on model predictions are demonstrated and discussed in detail in the original publication by Reymond et al. (2009). Combining data from a wide range of literature with a detailed description of the murine arterial anatomy, we have managed to translate the model into a murine setting, and to validate its predictions with *in vivo* flow

velocity, pressure and diameter waveforms measured in a large sample of mice. Despite its generic character, the resulting *in silico* model provides pressure and flow velocity waveforms that faithfully reproduce the actual wave characteristics at all arterial locations.

4.1 Overall model validation

To the best of our knowledge, the most elaborate model of the murine vasculature is the recent FSI model of an anesthetized mouse by Cuomo et al. (2015). This model was developed based on data from one single animal and incorporates the central aorta and its major branches. Table 3 compares our 1D model output to values predicted by Cuomo et al. (2015) and literature values. Cardiac output, stroke volume, ejection fraction and mean central pressure of the 1D model are within the range of published values. The central aPWV in both our 1D model and the 3D model of Cuomo et al. (2015) were above the range of aPWV values that have been measured with transit time methods. The reason is that in the 1D model we adapted the initial distensibility of the central aortic segments (Fig. 2) to match the central aortic compliance obtained by Guo and Kassab (2003). Transit time aPWV is not the most reliable measurement in mice since the relative measurement error on the transit distance is much larger than in humans (Cuomo et al., 2015; Trachet et al., 2015). Therefore, we judged that the global value of accumulated local *in vivo* pressure-diameter loops performed by Guo and Kassab (2003) yielded a more ac-

curate and trustworthy value for central aortic compliance. This hypothesis is further corroborated by the close match of our total volume compliance with the value that was obtained by Segers et al. using ventricular pressure-volume loops in n = 17 anesthetized mice (Segers et al., 2005), while the latter was not used as an input for the model.

4.2 Model validation at major arterial locations

When interpreting the model validation, it is important to keep in mind that the model is based on averaged data and by definition provides generic pressure and flow waveforms. While these aim to be representative for the average young, male laboratory mouse on a C57BL/6J background, they can only be compared qualitatively, and not quantitatively, to individual measurements. Ideally, full validation would require a mouse-specific approach, where all input parameters defining the model (geometry, elastic properties, peripheral resistances, varying elastance of the heart) would be tuned to each specific animal, after which predicted pressures and flows could be compared quantitatively with the measured waveforms in the same animal. Clearly, this is an impossible task, as the technical limitations hampering such precise measurements are the very reason we need an *in silico* model. Instead, we opted to compare the model predictions to measurements obtained in mice that were not used to define the input for the model (i.e., the local flow split, pressure and distensibility) at these locations.

In general, modeled flow velocities correspond well to the *in vivo* measurements (Fig. 3). However, while the modeled flow velocity predictions exhibit a gradual dampening along the main aortic segment, the *in vivo* measurements show a drop in the descending and thoracic aortic mean flow velocities, which is then followed by an increase of mean flow velocity in the abdominal aorta. Since there is no physiological reason for the velocity to drop locally, we believe that this discrepancy is due to a systematic underestimation of the measured velocity at the descending and thoracic arteries, rather than an error in the model. Given the curvature and branching of the local geometry in the descending aspects of the aortic arch, it is likely that the ultrasound measurements at these locations did not corre-

spond to the centerline velocity. Another possibility is that, because of the spatially skewed velocity profile at the descending aorta (Feintuch et al., 2007), the ultrasound measurement at the center of the vessel did not correspond to the peak velocity of an ideal, perfectly parabolic velocity profile. Both effects would lead to an underestimation of the measured velocities.

It is important to remark that the diameters shown in Figure 4 were not a direct output of the model, but were calculated a posteriori based on the nonlinear elastic instantaneous lumen area change under a distending pressure. Nevertheless, the diameter waveforms predicted by the model showed very good agreement with measured MMode diameter waveforms. Moreover, the general morphology of diameter and pressure waveforms was highly similar, as could be expected from literature (Hartley et al., 2005).

The pressure measurements were obtained in a set of C57BL/6J animals (n = 5). Despite the similar genetic background, age, gender and diet of the used experimental mice, pressure measurements showed significantly more inter and intra mice variability than the velocities or diameters (Tab. 2, Fig. 4). As discussed in previous work (Trachet et al., 2015), we hypothesize that this was most likely induced by (i) the invasive nature of the pressure measurements, as the inserted pressure probe alters local hemodynamics (Cuomo et al., 2015) since it blocks the femoral artery and significantly obstructs the flow in the distal part of the abdominal aorta, and (ii) the long period of anesthesia (around 45 min) required for the combination of surgery (probe insertion) and pressure measurements. Therefore, we judged the velocity and diameter model validations most trustworthy for validation purposes.

The modelled blood pressure in the tail was lower than the central blood pressure, and was found to be dependent on the amount of blood flow in the caudal artery. Higher blood flow to the caudal artery leads to higher viscous losses, resulting in a decrease of the mean blood pressure in the tail. As mice regulate the blood flow in the tail during thermoregulation, especially during anesthesia, these results confirm earlier findings that tail-cuff blood pressure measurements in anesthetized mice are to be interpreted with caution (Gordon, 1993; Zhao et al., 2011).

Tab. 3: Modeled hemodynamic parameters compared against the 3D model of Cuomo et al. (2015) and the range of reported physiological values

	CO, ml/min	SV, µl	EF, %	MAP, mmHg	aPWV, m/s	R, mmHg·µl⁻¹·s	C, µl·mmHg⁻¹	Z, mmHg·µl⁻¹·s
1D model	13.96	31.4	61	98	4.44	0.42	0.54	0.021
Cuomo et al., 2015	12.03	27.1	47	75	4.42	NA	NA	NA
Literature values	8-16[1,2]	17-36[1,2]	55-72[1]	81-105[1]	2.86-4.28[3,4,5*]	0.41 ± 0.13[6]	0.50 ± 0.15[6]	0.021 ± 0.005[6]

CO: cardiac output; SV: stroke volume; EF: ejection fraction; MAP: mean arterial pressure; aPWV: aortic pulse wave velocity; R: total systemic vascular resistance; C: total arterial compliance; Z: aortic characteristic impedance. Values for R, C, Z are means ± SD. Numbers refer to the publications reporting the values, i.e., [1]Cingolani and Kass, 2011, [2]Laflamme et al., 2012, [3]Hartley et al., 2000, [4]Reddy et al., 2003, [5]Wang et al., 2000, [6]Segers et al., 2005.
*values refer to both adult C57BL/6 WT mice and ApoE⁻/⁻ mice.

4.3 Model validation in small side branches

Model predictions in smaller branches could not be validated, since such measurements are technically very challenging: a rigid invasive pressure probe with a diameter of 0.4 mm cannot be inserted into the small side branches (Cuomo et al., 2015; Trachet et al., 2015), while high-frequency ultrasound flirts with the limits of the achievable resolution at these locations. Nevertheless, confirming previous results in the human 1D model (Reymond et al., 2009), we found that inclusion of the cerebral tree is necessary for the accuracy of model predictions in the carotid arteries (Fig. 5, panel A). Moreover we have recently demonstrated the previously undetected role of small branches in the early phase of cardiovascular pathology (Trachet et al., 2014a). Therefore, we decided to include the cerebral tree and other small branches in the model, despite the lack of proper validation. In the near future, improvements in imaging technology might lead to a more extensive validation that would include physiological measurements at these locations.

4.4 Anesthesia

All *in vivo* experiments (micro-CT, high-frequency ultrasound as well as invasive pressures) were performed under anesthesia, and so were all flow rates, cardiac parameters and local stiffness data that were extracted from literature. We did not attempt to convert all input and validation data into values that are representative for conscious mice. Instead, we chose to restrict the input of the model to measurements obtained under anesthesia, and thus *de facto* construct an *in silico* model representing the average anesthetized mouse. This choice was partly made for practical reasons, as it is neither possible nor ethically acceptable to perform *in vivo* measurements in conscious mice. Moreover a conversion of anesthetized to conscious data would have induced additional uncertainty and variability into the model. But we also believe that a model of anesthetized mice will prove more useful for the research community than a model for conscious mice, as it allows to investigate the influence of changes in anatomy or physiology *in silico* and compare the outcome to actual values measured *in vivo* (i.e., under anesthesia). Anesthesia slows down heart rate, reduces cardiac output (Janssen et al., 2004), and reduces pulse pressure, and it is important to take these factors into account when interpreting model predictions.

4.5 Genetic background

Model predictions were initially compared to a limited number (n = 5) of non-invasive flow velocity and invasive pressure measurements in C57BL/6J mice. To account for the biological variation in our initial validation data, we complemented them with velocity and diameter measurements from n = 47 ApoE^{-/-} that were readily available as baseline data from a study on abdominal aortic aneurysm (Trachet et al., 2015). This strategy enabled a more extensive, accurate and ethically justifiable validation of the model predictions since (i) many more animals and arterial locations could be included in the validation, and (ii) no additional animals needed to be sacrificed, which was after all the final goal of developing an *in silico* model.

It is, however, important to keep in mind that ApoE^{-/-} mice are genetically different from wild type C57BL/6J mice. These hy-

percholesterolemic mice develop atherosclerotic plaques when they are put on a Western diet, and aneurysms when they are infused with angiotensin II. At the time of the measurements, they were on a normal diet, at a young age, and had not yet been subjected to any surgical or pharmacological intervention. To account for any variability induced by the different genetic background, we compared micro-CT measurements of the main aorta and major branches of 3 ApoE^{-/-} mice with the arterial tree obtained in wild type mice. Since no significant difference in segment diameters or segment lengths could be detected, dimensions from both groups were combined in the final arterial tree. Since we did not observe any morphological differences between diameter and flow velocity waveforms obtained from both strains, and since genetic background, age, gender and diet were similar in both groups, we decided to combine all data into one single model.

4.6 Of mice and men

Despite the many similarities between human and murine arterial anatomy, it would be wrong to simply dismiss the murine cardiovascular system as a smaller and faster version of the human one, which is also the reason why we acquired mouse-specific input for the entire geometry and all boundary conditions, rather than downscaling the existing human model. For instance, while murine dimensions are much lower and murine heart rate is much higher, both blood viscosity and blood flow velocity are similar in mice and men. This has a number of implications. First of all, mice have a much lower Reynolds and Womersley number (Suo et al., 2007; Trachet et al., 2009) and thus murine flow is more laminar and organized than human flow (Trachet et al., 2011). In the numerical model of the human arterial tree, the Womersley number falls below 2.5 only in the radial, tibial and cerebral arteries. The Reynolds number drops below 175, which is the highest value it attains in the murine arterial tree, in the human cerebral segments, vertebral and external carotid arteries, as well as in the coronary arteries, the inner iliac and the inferior mesenteric artery. The Fåhraeus-Lindquist effect has been included in our model to account for the drop in apparent blood viscosity in small vessels, but appears to have no significant effect on our results, even in the smallest vessels of the cerebral arterial network.

Arterial pulse wave velocity values in mice are slightly lower but in the same order of magnitude as values measured in humans (Nichols et al., 1998), which means that pulse wave travels at similar speed in a much shorter system. In the human 1D model that formed the basis for this work, the aPWV was equal to 5.66 m/s (Boutouyrie and Vermeersch, 2010) and the heart rate was 75 bpm (1.25 Hz), resulting in a wavelength of 4.5 meters predicted by the wave equation. At the same time the central aorta in the human model measured 0.51 m, which is only 11.3% of the wavelength. In our murine model, the aPWV value of 4.44 m/s and a heart rate of 445 bpm (7.4 Hz) result in a wavelength of approximately 0.6 m. The central aorta in the murine model equals 47.3 mm, which corresponds to 7.9% of wavelength. Since the ratio of wavelength to total aortic length is similar in the two cases, we would expect similar wave propagation behavior. However, there is no pulse

pressure amplification in the mouse model as we move from the proximal aorta (PP = 41.7 mmHg) to the iliac bifurcation (PP = 40.2 mmHg). Instead, the pulse pressure is gradually dampened from the heart to the periphery. At the same time the model yields a drop in mean pressure of 5.5 mmHg from the proximal aorta to the distal abdominal part. On the other hand, when assuming inviscid flow, the model does exhibit a pulse pressure amplification of 36 mmHg in the proximal aorta to 42 mmHg at the iliac bifurcation, which is similar to the pulse pressure amplification observed in the human model. The high frictional losses thus override the effect of pulse pressure amplification in the mouse.

4.7 Model limitations and possibilities for improvement

Limitations related to the *in vivo* measurements (anesthesia, inter-mouse variability, genetic background) have been discussed above. From a modeling point of view, we believe that our model is state-of-the-art, as we managed to translate all features of the state-of-the-art 1D-model of the human arterial tree into a murine setting. Both the assets and the limitations of our model are therefore comparable to those of the human 1D model. The model neglects the venous circulation, the pulmonary circulation and the circulation of cerebrospinal fluid surrounding intracranial arteries. Windkessel models employed in the cerebral circulation are based on assumptions and should be investigated in more detail. The varying elastance curve may not be invariant in the presence of cardiovascular disease (Jegger et al., 2007), and the varying elastance model may not be the most appropriate to account for changes in pressure and volume during the cardiac cycle in anesthetized mice (Claessens et al., 2006). Viscoelastic parameters were obtained from a limited number of canine arteries (Bergel, 1961), and additional datasets on aortic wall viscoelasticity are needed to refine this aspect for both the human and the murine model. Finally, the input and validation of the model have been restricted to young male mice, while the cardiovascular anatomy and physiology change significantly with age as well as gender (Reddy et al., 2003). Future work will focus on the development of dedicated age- and gender dependent models, in which arterial dimensions, wall properties, peripheral impedances and cardiac function will be appropriately adjusted.

4.8 Conclusions and future work

We presented a versatile numerical model of the systemic arterial tree in mice. Detailed measurements of anatomy (obtained from *in vivo* micro-CT measurements) and physiology (obtained from high-frequency ultrasound measurements and literature data) were combined with a 1-D implementation of the Navier-Stokes equations to predict pressure and flow waveforms in 85 different branches. The output of the model has been shown to correspond well with pressure, diameter as well as velocity measurements obtained in mice that were not used as an input for the model.

At a time of strong ethical considerations over animal testing, we believe that computational models have an important role to play. While specific biological experiments can and will

obviously never be replaced by generic modelling results, our versatile 1D model is perfectly suited to serve as an alternative for *in vivo* proof-of-concept studies. Rather than performing cumbersome invasive measurements that often require to sacrifice the animals in order to gain insight into the physiology of altered experimental conditions (e.g., in case of the ligation of a specific artery or the increase of aortic stiffness), a wide range of different physiological conditions can be simulated in the model without sacrificing a single animal. The ability to simulate cardiovascular pathology (e.g., aortic valve insufficiency, aortic aneurysm, stenosis, hypertension) or operative measures affecting the arterial anatomy (e.g., aortic ligation, castration, amputation) prior to or instead of sacrificing animals, can lead to the reduction and ultimate replacement of the amount of sacrificed animals in (the pilot stage of) newly developed experimental techniques and thus facilitate the implementation of the 3R's principle in research practice. The model could also lead to the derivation of central pressures from tail cuff measurements, through a transfer function.

References

Agianniotis, A. and Stergiopulos, N. (2012). Wall properties of the apolipoprotein E-deficient mouse aorta. *Atherosclerosis 223*, 314-320. http://dx.doi.org/10.1016/j.atherosclerosis. 2012.06.014

Avolio, A. P. (1980). Multi-branched model of the human arterial system. *Med Biol Eng Comput 18*, 709-718. http://dx.doi. org/10.1007/BF02441895

Bergel, D. H. (1961). The dynamic elastic properties of the arterial wall. *J Physiol 156*, 458-469. http://dx.doi.org/10.1113/jphysiol.1961.sp006687

Bessems, D., Rutten, M. and Van De Vosse, F. (2007). A wave propagation model of blood flow in large vessels using an approximate velocity profile function. *J Fluid Mechanics 580*, 145-168. http://dx.doi.org/10.1017/S0022112007005344

Bolduc, V., Baraghis, E., Duquette, N. et al. (2012). Catechin prevents severe dyslipidemia-associated changes in wall biomechanics of cerebral arteries in LDLr$^{-/-}$:hApoB$^{+/+}$ mice and improves cerebral blood flow. *Am J Physiol Heart Circ Physiol 302*, H1330-1339. http://dx.doi.org/10.1152/ajpheart.01044.2011

Boutouyrie, P. and Vermeersch, S. J. (2010). Determinants of pulse wave velocity in healthy people and in the presence of cardiovascular risk factors: Establishing normal and reference values. *Eur Heart J 31*, 2338-2350. http://dx.doi.org/10.1093/eurheartj/ehq165

Campens, L., Renard, M., Trachet, B. et al. (2015). Intrinsic cardiomyopathy in marfan syndrome: Results from in- and ex-vivo studies of the Fbn1(C1039G/+) model and longitudinal findings in humans. *Pediatr Res 78*, 256-263. http://dx.doi. org/10.1038/pr.2015.110

Casteleyn, C., Trachet, B., Van Loo, D. et al. (2010). Validation of the murine aortic arch as a model to study human vascular diseases. *J Anat 216*, 563-571. http://dx.doi.org/10.1111/j.1469-7580.2010.01220.x

Cingolani, O. H. and Kass, D. A. (2011). Pressure-volume relation analysis of mouse ventricular function. *Am J Phys-*

iol Heart Circ Physiol 301, H2198-2206. http://dx.doi.org/10.1152/ajpheart.00781.2011

Claessens, T. E., Georgakopoulos, D., Afanasyeva, M. et al. (2006). Nonlinear isochrones in murine left ventricular pressure-volume loops: How well does the time-varying elastance concept hold? *Am J Physiol Heart Circ Physiol 290*, H1474-1483. http://dx.doi.org/10.1152/ajpheart.00663.2005

Cuomo, F., Ferruzzi, J., Humphrey, J. D. et al. (2015). An experimental-computational study of catheter induced alterations in pulse wave velocity in anesthetized mice. *Ann Biomed Eng 43*, 1555-1570. http://dx.doi.org/10.1007/s10439-015-1272-0

De Man, B., Nuyts, J., Dupont, P. et al. (2001). An iterative maximum-likelihood polychromatic algorithm for CT. *IEEE Trans Med Imaging 20*, 999-1008. http://dx.doi.org/10.1109/42.959297

De Wilde, D., Trachet, B., Van der Donckt, C. et al. (2015). Vulnerable plaque detection and quantification with gold particle-enhanced computed tomography in atherosclerotic mouse models. *Mol Imaging 14*, 9-19.

Fahraeus, R. and Lindqvist, T. (1930). The viscosity of the blood in narrow capillary tubes. *Am J Physiol 96*, 562-568.

Feintuch, A., Ruengsakulrach, P., Lin, A. et al. (2007). Hemodynamics in the mouse aortic arch as assessed by MRI, ultrasound, and numerical modeling. *Am J Physiol Heart Circ Physiol 292*, 884-892. http://dx.doi.org/10.1152/ajpheart.00796.2006

Fitch, R. M., Rutledge, J. C., Wang, Y.-X. et al. (2006). Synergistic effect of angiotensin II and nitric oxide synthase inhibitor in increasing aortic stiffness in mice. *Am J Physiol Heart Circ Physiol 290*, H1190-1198. http://dx.doi.org/10.1152/ajpheart.00327.2005

Georgakopoulos, D., Mitzner, W. A., Chen, C. H. et al. (1998). In vivo murine left ventricular pressure-volume relations by miniaturized conductance micromanometry. *Am J Physiol 274*, H1416-1422.

Gordon, C. J. (1993). *Temperature Regulation in Laboratory Rodents*. Cambridge University Press. http://dx.doi.org/10.1017/cbo9780511565595

Grieve, D. J., Cave, A. C., Byrne, J. et al. (2004). Analysis of ex vivo left ventricular pressure-volume relations in the isolated murine ejecting heart. *Exp Physiol 89*, 573-582. http://dx.doi.org/10.1113/expphysiol.2004.027573

Grupp, I. L., Subramaniam, A., Hewett, T. E. et al. (1993). Comparison of normal, hypodynamic, and hyperdynamic mouse hearts using isolated work-performing heart preparations. *Am J Physiol 265*, H1401-1410.

Guo, X. and Kassab, G. S. (2003). Variation of mechanical properties along the length of the aorta in C57bl/6 mice. *Am J Physiol Heart Circ Physiol 285*, H2614-2622. http://dx.doi.org/10.1152/ajpheart.00567.2003

Guo, X., Oldham, M. J., Kleinman, M. T. et al. (2006). Effect of cigarette smoking on nitric oxide, structural, and mechanical properties of mouse arteries. *Am J Physiol Heart Circ Physiol 291*, H2354-2361. http://dx.doi.org/10.1152/ajpheart.00376.2006

Hartley, C., Reddy, A., Entman, M. et al. (2005). Characteri-
zation of arterial wave propagation and reflection in mice. *Conf Proc IEEE Eng Med Biol Soc 1*, 601-604. http://dx.doi.org/10.1109/IEMBS.2005.1616484

Herold, V., Parczyk, M., Mörchel, P. et al. (2009). In vivo measurement of local aortic pulse-wave velocity in mice with MR microscopy at 17.6 Tesla. *Magn Reson Med 61*, 1293-1299. http://dx.doi.org/10.1002/mrm.21957

Holenstein, R., Niederer, P. and Anliker, M. (1980). A viscoelastic model for use in predicting arterial pulse waves. *J Biomech Eng 102*, 318-325. http://dx.doi.org/10.1115/1.3138229

Hoyt, R. E., Hawkins, J. V., St Clair, M. B. et al. (2007). Mouse Physiology. In J. G. Fox, M. T. Davisson, F. W. Quimby et al. (eds.), *The Mouse in Biomedical Research* (23-90). Vol. 3. Elsevier Inc.

Janssen, B. J., De Celle, T., Debets, J. J. et al. (2004). Effects of anesthetics on systemic hemodynamics in mice. *Am J Physiol Heart Circ Physiol 287*, H1618-1624. http://dx.doi.org/10.1152/ajpheart.01192.2003

Jegger, D., Mallik, A. S., Nasratullah, M. et al. (2007). The effect of a myocardial infarction on the normalized time-varying elastance curve. *J Appl Physiol (1985) 102*, 1123-1129. http://dx.doi.org/10.1152/japplphysiol.00976.2006

Langewouters, G. J. (1982). Visco-elasticity of the human aorta in vitro in relation to pressure and age. PhD Thesis: Free University of Amsterdam, The Netherlands.

Langewouters, G. J., Wesseling, K. H. and Goedhard, W. J. (1984). The static elastic properties of 45 human thoracic and 20 abdominal aortas in vitro and the parameters of a new model. *J Biomech 17*, 425-435. http://dx.doi.org/10.1016/0021-9290(84)90034-4

Le, V. P., Knutsen, R. H., Mecham, R. P. et al. (2011). Decreased aortic diameter and compliance precedes blood pressure increases in postnatal development of elastin-insufficient mice. *Am J Physiol Heart Circ Physiol 301*, H221-229. http://dx.doi.org/10.1152/ajpheart.00119.2011

Lips, D. J., van der Nagel, T., Steendijk, P. et al. (2004). Left ventricular pressure-volume measurements in mice: Comparison of closed-chest versus open-chest approach. *Basic Res Cardiol 99*, 351-359. http://dx.doi.org/10.1007/s00395-004-0476-5

Luo, J., Fujikura, K., Tyrie, L. S. et al. (2009). Pulse wave imaging of normal and aneurysmal abdominal aortas in vivo. *IEEE Trans Med Imaging 28*, 477-486. http://dx.doi.org/10.1109/TMI.2008.928179

Mynard, J. P. and Smolich, J. J. (2015). One-dimensional haemodynamic modeling and wave dynamics in the entire adult circulation. *Ann Biomed Eng 43*, 1443-1460. http://dx.doi.org/10.1007/s10439-015-1313-8

Nemoto, S., DeFreitas, G., Mann, D. L. and Carabello, B. A. (2002). Effects of changes in left ventricular contractility on indexes of contractility in mice. *Am J Physiol Heart Circ Physiol 283*, H2504-2510. http://dx.doi.org/10.1152/ajpheart.00765.2001

Nichols, W., O'Rourke, M. and Vlachopoulos, C. (1998). *McDonald's Blood Flow in Arteries: Theoretical, Experimental*

and Clinical Principles. 4th edition. New York: Oxford University Press.

Nichols, W., O'Rourke, M. and Vlachopoulos, C. (2011). Contours of Pressure and Flow Waves in Arteries. In *McDonald's Blood Flow in Arteries – Theoretical, experimental and clinical principles* (225-253). Boca Raton: CRC Press, Taylor & Francis Group.

Pacher, P., Nagayama, T., Mukhopadhyay, P. et al. (2008). Measurement of cardiac function using pressure-volume conductance catheter technique in mice and rats. *Nat Protoc 3*, 1422-1434. http://dx.doi.org/10.1038/nprot.2008.138

Pennacchio, L. a. (2003). Insights from Human/mouse Genome Comparisons. *Mamm Genome 14*, 429-436. http://dx.doi.org/10.1007/s00335-002-4001-1

Rabben, S. I., Bjærum, S., Sørhus, V. et al. (2002). Ultrasound-based vessel wall tracking: An auto-correlation technique with RF center frequency estimation. *Ultrasound Med Biol 28*, 507-517. http://dx.doi.org/10.1016/S0301-5629(02)00487-8

Reddy, A. K., Li, Y.-H., Pham, T. T. et al. (2003). Measurement of aortic input impedance in mice: Effects of age on aortic stiffness. *Am J Physiol Heart Circ Physiol 285*, H1464-1470. http://dx.doi.org/10.1152/ajpheart.00004.2003

Reed, J. C. and Herold, K. C. (2015). Thinking bedside at the bench: The NOD mouse model of T1DM. *Nat Rev Endocrinol 11*, 308-314. http://dx.doi.org/10.1038/nrendo.2014.236

Reymond, P., Merenda, F., Perren, F. et al. (2009). Validation of a one-dimensional model of the systemic arterial tree. *Am J Physiol Heart Circ Physiol 297*, H208-222. http://dx.doi.org/10.1152/ajpheart.00037.2009

Sagawa, K. (1981). The end-systolic pressure-volume relation of the ventricle: Definition, modifications and clinical use. *Circulation 63*, 1223-1227. http://dx.doi.org/10.1161/01.CIR.63.6.1223

Secomb, T. W. and Pries, A. R. (2013). Blood viscosity in microvessels: Experiment and theory. *C R Phys 14*, 470-478. http://dx.doi.org/10.1016/j.crhy.2013.04.002

Segers, P., Stergiopulos, N. and Westerhof, N. (2000). Quantification of the contribution of cardiac and arterial remodeling to hypertension. *Hypertension 36*, 760-765. http://dx.doi.org/10.1161/01.HYP.36.5.760

Segers, P., Stergiopulos, N., Westerhof, N. et al. (2002). Relation of effective arterial elastance to arterial system properties. *Am J Physiol Heart Circ Physiol 282*, 1041-1046. http://dx.doi.org/10.1152/ajpheart.00764.2001

Segers, P., Georgakopoulos, D., Afanasyeva, M. et al. (2005). Conductance catheter-based assessment of arterial input impedance, arterial function, and ventricular-vascular interaction in mice. *Am J Physiol Heart Circ Physiol 288*, H1157-1164. http://dx.doi.org/10.1152/ajpheart.00414.2004

Senzaki, H., Chen, C. and Kass, D. (1996). Single-beat estimation of end-systolic pressure-volume relation in humans. A new method with the potential for noninvasive application. *Circulation 94*, 2497-2506. http://dx.doi.org/10.1161/01.CIR.94.10.2497

Sherwin, S. J., Franke, V., Peiro, J. et al. (2003). One-dimensional modelling of a vascular network in space-time variables. *J Eng Math 47*, 217-250. http://dx.doi.org/10.1023/B:ENGI.0000007979.32871.e2

Shioura, K. M., Geenen, D. L. and Goldspink, P. H. (2007). Assessment of cardiac function with the pressure-volume conductance system following myocardial infarction in mice. *Am J Physiol Heart Circ Physiol 293*, H2870-2877. http://dx.doi.org/10.1152/ajpheart.00585.2007

Stergiopulos, N., Young, D. F. and Rogge, T. R. (1992). Computer simulation of arterial flow with applications to arterial and aortic stenoses. *J Biomech 25*, 1477-1488. http://dx.doi.org/10.1016/0021-9290(92)90060-E

Stergiopulos, N., Westerhof, B. E., Westerhof, N. et al. (1999). Total arterial inertance as the fourth element of the windkessel model. *Am J Physiol 276*, H81-88.

Sugihara-Seki, M. and Fu, B. M. (2005). Blood flow and permeability in microvessels. *Fluid Dyn Res 37, Spec. Issue 1-2*, 82-132. http://dx.doi.org/10.1016/j.fluiddyn.2004.03.006

Suo, J., Ferrara, D. E., Sorescu, D. et al. (2007). Hemodynamic shear stresses in mouse aortas: Implications for atherogenesis. *Arterioscler, Thromb Vasc Biol 27*, 346-351. http://dx.doi.org/10.1161/01.ATV.0000253492.45717.46

Tian, L., Wang, Z., Lakes, R. S. et al. (2013). Comparison of approaches to quantify arterial damping capacity from pressurization tests on mouse conduit arteries. *J Biomech Eng 135*, 54504. http://dx.doi.org/10.1115/1.4024135

Trachet, B., Swillens, A., Van Loo, D. et al. (2009). The influence of aortic dimensions on calculated wall shear stress in the mouse aortic Arch. *Comput Methods Biomech Biomed Engin 12*, 491-499. http://dx.doi.org/10.1080/10255840802695445

Trachet, B., Bols, J., De Santis, G. et al. (2011). The impact of simplified boundary conditions and aortic Arch inclusion on CFD simulations in the mouse aorta: A comparison with mouse-specific reference data. *J Biomech Eng 133*, 121006. http://dx.doi.org/10.1115/1.4005479

Trachet, B., Fraga-Silva, R. A., Piersigilli, A. et al. (2014a). Dissecting abdominal aortic aneurysm in Ang II-infused mice: Suprarenal branch ruptures and apparent luminal dilatation. *Cardiovasc Res 105*, 213-222. http://dx.doi.org/10.1093/cvr/cvu257

Trachet, B., Renard, M., Van der Donckt, C. et al. (2014b). Longitudinal follow-up of ascending versus abdominal aortic aneurysm formation in angiotensin II-infused ApoE$^{-/-}$ Mice. *Artery Res 8*, 16-23. http://dx.doi.org/10.1016/j.artres.2014.01.001

Trachet, B., Fraga-Silva, R. A., Londono, F. J. et al. (2015). Performance comparison of ultrasound-based methods to assess aortic diameter and stiffness in normal and aneurysmal mice. *PLoS One 10*, e0129007. http://dx.doi.org/10.1371/journal.pone.0129007

Treuting, P. M., Dintzis, S. M. and Montine, K. S. (2012). Introduction. In Treuting, P. M. and Dintzis, S. M. (eds.), *Comparative Anatomy and Histology – A Mouse and Human Atlas* (1-6). London, UK: Elsevier Inc. http://dx.doi.org/10.1016/B978-0-12-381361-9.00001-9

Van der Donckt, C., Van Herck, J. L., Schrijvers, D. M. et al. (2014). Elastin fragmentation in atherosclerotic mice leads to intraplaque neovascularization, plaque rupture, myocardial infarction, stroke, and sudden death. *Eur Heart J 36*, 1049-1058. http://dx.doi.org/10.1093/eurheartj/ehu041

Vardoulis, O., Coppens, E., Martin, B. et al. (2011). Impact of aortic grafts on arterial pressure: A computational fluid dynamics study. *Eur J Vasc Endovasc Surg 42*, 704-710. http://dx.doi.org/10.1016/j.ejvs.2011.08.006

Vardoulis, O., Papaioannou, T. G. and Stergiopulos, N. (2012). On the estimation of total arterial compliance from aortic pulse wave velocity. *Ann Biomed Eng 40*, 2619-2126. http://dx.doi.org/10.1007/s10439-012-0600-x

Wagenseil, J. E., Nerurkar, N. L., Knutsen, R. H. et al. (2005). Effects of elastin haploinsufficiency on the mechanical behavior of mouse arteries. *Am J Physiol Heart Circ Physiol 289*, H1209-1217. http://dx.doi.org/10.1152/ajpheart.00046.2005

Wang, Y.-X. (2005). Cardiovascular functional phenotypes and pharmacological responses in apolipoprotein E deficient mice. *Neurobiol Aging 26*, 309-316. http://dx.doi.org/10.1016/j.neurobiolaging.2004.06.018

Wemple, R. R. and Mockros, L. (1972). Pressure and flow in the systemic arterial system. *J Biomech 5*, 629-641. http://dx.doi.org/10.1016/0021-9290(72)90035-8

Westerhof, N., Lankhaar, J.-W. and Westerhof, B. (2009). The arterial windkessel. *Med Biol Eng Comput 47*, 131-141. http://dx.doi.org/10.1007/s11517-008-0359-2

Williams, R., Needles, A., Cherin, E. et al. (2007). Noninvasive ultrasonic measurement of regional and local pulse-wave velocity in mice. *Ultrasound Med Biol 33*, 1368-1375. http://dx.doi.org/10.1016/j.ultrasmedbio.2007.03.012

Yamaguchi, N., Takahashi, N., Xu, L. et al. (2007). Early cardiac hypertrophy in mice with impaired calmodulin regulation of cardiac muscle Ca^{2+} release channel. *J Clin Invest 117*, 1344-1353. http://dx.doi.org/10.1172/JCI29515DS1

Yang, B., Larson, D. F. and Watson, R. (1999). Age-related left ventricular function in the mouse: Analysis based on in vivo pressure-volume relationships. *Am J Physiol 277*, H1906-1913.

Zhao, X., Ho, D., Gao, S. et al. (2011). Arterial pressure monitoring in mice. *Curr Protoc Mouse Biol 1*, 105-122. http://dx.doi.org/10.1002/9780470942390.mo100149

Conflict of interest statement

None declared.

Correspondence to

Lydia Aslanidou
LHTC, STI-IBI, EPFL
Station 17
1015 Lausanne
Switzerland
Phone: 0041 79 953 00 78
e-mail: lydia.aslanidou@epfl.ch